

Evaluation of the AMSR-E Data Calibration over Land

E. Njoku¹, T. Chan¹, W. Crosson², A. Limaye²

¹Jet Propulsion Laboratory
California Institute of Technology
Pasadena, CA 91109

²Global Hydrology and Climate Center
National Space Science and Technology Center
Huntsville, AL 35805

April 13, 2004

Prepared for submission to:
Italian Journal of Remote Sensing

Abstract

Land observations by the Advanced Microwave Scanning Radiometer for the Earth Observing System (AMSR-E), particularly of soil and vegetation moisture changes, have numerous applications in hydrology, ecology and climate. Quantitative retrieval of soil and vegetation parameters relies on accurate calibration of the brightness temperature measurements. Analyses of the spectral and polarization characteristics of early versions of the AMSR-E data revealed significant calibration biases over land at 6.9 GHz. The biases were estimated and removed in the current archived version of the data. Radio-frequency interference (RFI) observed at 6.9 GHz is more difficult to quantify however. A calibration analysis of AMSR-E data over land is presented in this paper for a complete annual cycle from June 2002 through September 2003. The analysis indicates the general high quality of the data for land applications (except for RFI), and illustrates seasonal trends of the data for different land surface types and regions.

Introduction

The Advanced Microwave Scanning Radiometer for the Earth Observing System (AMSR-E) was launched in May 2002 on NASA's Aqua satellite [Parkinson, 2003]. The instrument was developed for NASA by the Japan Aerospace Exploration Agency (JAXA) [Kawanishi et al., 2003]. AMSR-E provides observations of several water-related geophysical parameters of interest to hydrology, ecology and climate. Over land, measurements of soil moisture and vegetation water content rank high on the list of measurements needed for improved weather and climate forecasting and for monitoring floods, droughts, and ecosystem dynamics. Algorithms to derive soil and vegetation parameters have been developed and are being evaluated using AMSR-E data [Njoku et al., 2000; Paloscia et al., 2001; Owe et al., 2001; Njoku et al., 2003]. Quantitative retrieval of geophysical parameters requires accurate radiometric data calibration to avoid biases in the estimates. Calibration offsets that are stable in space and time can be relatively easily estimated and adjusted either in a revised instrument calibration or in the

geophysical retrieval algorithms. However, spatial and temporal variations in the instrument calibration are less easily removed, and the residual calibration errors can lead to spurious trends in the retrieved geophysical parameters. The stability of the relative calibration offsets between channels is particularly important for multichannel algorithms that rely on spectral or polarization differences to discriminate between different geophysical parameters.

In previous satellite missions, homogeneous extended targets over ocean and land regions have been used for on-orbit calibration assessments of microwave radiometers. The brightness temperatures of the extended targets are relatively stable and can be estimated reasonably accurately for comparison with the satellite observations. Such targets include tropical forests, oceans, deserts, and Antarctic sites. By analyzing observations over these targets continuously during the mission, calibration offsets and their long-term stability and trends can be estimated and corrected [Hollinger et al., 1990; Tsai et al., 1999; Ruf, 2000; Wentz et al., 2001].

In this paper we investigate the AMSR-E data characteristics and calibration over land by examining statistics of the brightness temperatures, spectral differences, and polarization differences over geographical regions including forests, deserts, and land ice. The intent is to evaluate the quality and space-time variability of the current version of AMSR-E calibrated and archived data for retrieval of land geophysical quantities.

Two versions of AMSR-E level 2A data were used in this study. The first version, designated 'X1', was made available to the AMSR-E science team shortly after launch for algorithm and product evaluation during the initial evaluation phase. The second version, designated 'B01', was the result of an improved calibration, and data of this version were made available for public release as of September 2003 through the AMSR-E data archive at the National Snow and Ice Data Center in Boulder (NSIDC), Colorado (<http://nsidc.org/daac/amsr/>). Early analyses of the 'X1' data showed consistently high values of brightness temperature in the 6.9 GHz channels over land, indicating a high calibration bias. Calibration assessments performed by the AMSR-E team led to implementation of a modified AMSR-E calibration algorithm, resulting in an improved

calibration version 'B01' data [Wentz et al., 2003]. The current analysis of the 'B01' data indicates that the calibration biases appear to have been removed satisfactorily for land applications. However, some differences may exist between the calibrations of the 'B01' data available through NSIDC and the AMSR-E brightness temperature data made available through the EOC data center in Japan [Kawanishi et al., 2003] since the latter were processed using a different calibration correction.

In the following sections of the paper we review briefly the AMSR-E instrument and data processing. We then discuss the procedure used to estimate calibration biases in the 'X1' 6.9 GHz data using homogeneous forest targets. Subsequent sections of the paper are devoted to analyses of the 'B01' data to assess the quality of the currently archived data for AMSR-E land applications.

Instrument and Data

The AMSR-E instrument has six frequencies in the range 6.9 to 89 GHz, with dual polarization (Table 1). The 6.9, 10.7, 18.7 and 36.5 GHz frequencies are of primary interest for surface sensing since the 23.8 and 89 GHz frequencies are significantly affected by atmospheric water vapor and clouds. The antenna system consists of a 1.6-m-diameter offset-fed parabolic reflector with six feed horns (there are two feed horns at 89 GHz and one is shared between the 18 and 23 GHz frequencies). The beams are offset at 47.5° from nadir, and the antenna system rotates about the nadir axis at 40 rpm. The beams view the surface at a constant incidence angle of approximately 55° across a swath width of 1450 km. The sub-satellite-track Equator-crossing times are approximately 1:30 pm and 1:30 am local solar time. However, data samples acquired at opposite sides of the 1445-km swath vary by 50 minutes or more in local solar time.

As described by Kawanishi et al. [2003] the AMSR-E instrument calibration assembly includes a cold-sky mirror (CSM) and a high-temperature noise source (HTS) made of microwave absorber material with emissivity close to 1. These calibration targets are fixed to the spacecraft structure and intercept the beam path between the feed horns and

reflector as the antenna system rotates, providing cold and warm reference calibration measurements. The 3-K cosmic background radiation reflected into the feed horns by the CSM provides the cold reference. The HTS is temperature-controlled and its temperature is monitored using eight platinum resistance thermistors (PRTs) distributed over the target, providing a warm reference target. Calibrated antenna temperatures are computed by linear interpolation using measurements of the two known references. The radiometer system calibration also includes corrections for antenna cross-polarization and sidelobes viewing cold sky, such that the outputs represent calibrated Earth-view brightness temperatures. These are often considered to be 3-dB footprint brightness temperatures, although this is only an approximation since corrections are not made for energy received from the region outside the 3-dB footprint but within the Earth horizon. A source of potential calibration error was discovered during the pre-launch calibration testing by JAXA of the AMSR-E instrument. Temperature gradients were detected in the HTS during thermal cycling that were not adequately measured by the PRT sensors. This introduced significant uncertainty into knowledge of the HTS calibration reference temperature. Schedule and resource limitations prevented a redesign of the HTS prior to launch [Kawanishi et al., 2003].

In the post-launch data processing flow, AMSR-E level 1A data (uncalibrated, but with calibration data and coefficients included) are generated by JAXA and sent via the Jet Propulsion Laboratory in Pasadena, CA to the AMSR-E level 2A processing center at Remote Sensing Systems (RSS) in Santa Rosa, California. The calibrated level 2A brightness temperatures [Ashcroft and Wentz, 2000] are used as the basis for the higher-level geophysical processing to level 2B and level 3 data products, which takes place at the NASA Marshall Space Flight Center (MSFC) in Huntsville, Alabama. The AMSR-E data products are made available to the public via the NSIDC Distributed Active Archive Center (DAAC) in Boulder, Colorado.

An empirical approach was used in the level 2A processing to mitigate the uncertainty in knowledge of the on-orbit HTS reference temperature. This approach was developed by RSS [Wentz et al., 2003] and involved estimating the HTS reference temperature by

using a real-time external database of operational satellite measurements acquired over the ocean. The operational satellite geophysical parameter measurements, co-registered to the AMSR-E data, were used with a radiative transfer model to compute the intensity of radiation entering the AMSR-E feed horns. In essence this provides an ocean-target calibration point. A two-point linear extrapolation based on the cold-sky mirror and ocean-target calibration points provides an estimate of the reference temperature of the HTS target. The reference temperature is then correlated with variations in the HTS thermistors to obtain an expression for the reference temperature as a function of the thermistor measurements. This procedure was used as the basis for version 'X1' of the AMSR-E data. A modification to the above approach for the 6.9 GHz channels was later implemented by RSS to correct the warm calibration biases observed in the brightness temperatures (TBs) over land (discussed later in this paper). This modification was used to generate the version 'B01' data. For the analysis described in this paper, we binned the level 2A TB data into daily 25-km grids, separately for ascending and descending passes, as described in [Njoku et al., 2003]. This was done to generate time series of data using both the 'X1' and 'B01' versions of the data.

To examine the temporal and geographic characteristics of the brightness temperature data nineteen locations were selected for investigation, shown in Figure 1. The center coordinates are listed in Table 2. The locations were selected over tropical and boreal forests (dense vegetation), deserts (bare surface), grasslands, and Sahel (sparse vegetation) to investigate the characteristics of different classes of homogeneous land surface types. One ice sheet location was selected in the Antarctic plateau. The locations were chosen to be free of radio-frequency interference (RFI) where possible. RFI will be discussed later in the paper. At each location, for each day of coverage, a 3x3 (75x75 km) array of gridded data were extracted from the ascending and descending daily brightness temperature (TB) grids, and the daily means and standard deviations were computed.

Analysis of 'X1' Data

To assess the absolute brightness temperature calibration of the 'X1' data over land, data from tropical forests sites were analyzed. Homogeneous tropical forests are the closest land-surface analog to an extended blackbody target and can be used to assess the TB calibration at the warm end of the land brightness temperature range. Figure 2 shows the mean brightness temperatures of the 'X1' data over two forest sites at Salonga (Zaire) and Curua (Brazil), at the frequencies of 6.9, 10.7, 18.7 and 36.5 GHz, averaged over the June through August 2002 time period. The 7 to 10 K TB difference between ascending and descending passes is expected, due to the difference in canopy temperatures between the 1:30 pm (ascending) and 1:30 am (descending) overpass times. For a given polarization and overpass time, the TB values at 6.9 GHz are observed to be significantly higher than the values at the other frequencies. This unexpected spectral feature was observed consistently at all land sites. If the forest were a blackbody of uniform temperature, with no overlying atmosphere, the observed spectrum would be flat. However, vegetation scattering, nonuniform temperature, and atmospheric effects could be expected to introduce spectral differences. To examine the possible effects of atmospheric water vapor and oxygen, a radiative transfer model was used to compute the expected differences between brightness temperatures with and without an atmospheric layer. The computations assumed a standard tropical atmosphere with two cases of precipitable water (5 cm and 7 cm), equal ground and surface air temperatures of 300 K, and three cases of different surface emissivities (0.94, 0.96, 0.98). The results, shown in Figure 3, illustrate that the atmosphere can either increase (positive difference) or decrease (negative difference) the observed TB, depending on whether the emission contribution of the atmosphere is greater or less than the attenuation by the atmosphere of the surface brightness temperature. This is a function of the surface emissivity, the atmospheric temperature and water vapor profiles, and the frequency dependence of the atmospheric absorption coefficient. The emissivity depends on absorption and scattering in the vegetation. Its frequency dependence is influenced by the dimensions of the canopy and branch constituents relative to the wavelength, and their shapes, orientations and water content. Figure 3 shows that differences of a few Kelvins between the 10.7, 18.6, and 36.5 GHz frequencies observed in Figure 2 can be explained by atmospheric effects and

surface emissivities varying in the 0.94–0.98 range. However, the elevation of the 6.9 GHz TBs by about 7 K relative to the 10.65 GHz TBs is clearly anomalous.

To investigate this further, land surface temperatures (LSTs) from the Aqua Moderate-resolution Imaging Spectroradiometer (MODIS) instrument were used to normalize the AMSR-E TB data and compute emissivities at 6.9 GHz and 10.6 GHz. The MODIS level 3 LST data were acquired for dates when cloud-free data were available. The LSTs were derived using a generalized split-window algorithm to correct for atmosphere and emissivity effects of known land cover types [Wan and Li, 1997; Wan, 1999]. The LST data have a spatial resolution of 1 km and an estimated accuracy of 1 K [Wan et al., 2004]. For this study, cloud-free MODIS LST data were extracted and averaged over seven of the 75 x 75 km AMSR-E study sites listed in Table 2. LSTs within the study sites did not show significant variability, with standard deviations for each site being less than 3 K. The MODIS and AMSR-E data are coincident in time since the instruments are on the same satellite. Figures 4 (a) and (b) show time-series of the nighttime overpass MODIS LSTs and the 6.9 GHz and 10.6 GHz AMSR-E TBs at V and H polarizations, over the Salonga, Zaire tropical forest site. Nighttime data were used since the MODIS surface temperature and the deeper-sampled microwave temperature in the canopy are more likely to be similar at night than during the day. Also shown in these figures are the 6.9 GHz TBs with 7 K subtracted. The resulting very close match with the 10.7 GHz TBs suggests a consistent 7 K calibration error in the 6.9 GHz V- and H-polarized TB data at this site. Analyses of data over the other forest sites showed biases of similar magnitude. Emissivities derived by normalizing the AMSR-E TBs with the MODIS LSTs are shown in Figures 4(c) and (d). The 10.7 GHz emissivities are quite stable in the 0.95–0.97 range, with V-pol values being approximately 0.01 higher than H-pol. The 6.9 GHz emissivities are consistently higher by approximately 0.03 than those at 10.7 GHz.

As discussed earlier, the 'X1' calibration was developed using ocean data and its performance was verified over the ocean at all frequencies. However, over land, the above analysis showed that the 'X1' 6.9 GHz AMSR-E TBs were biased consistently high relative to 10.7 GHz by about 7 K. After considering the various instrument possibilities

that could cause such a bias, it was concluded by RSS that a non-linear response function for the 6.9 GHz radiometer was the probable cause. A non-linear term was therefore added to the calibration equation for the 6.9 GHz frequency [Wentz, 2004]. This modified calibration was used in processing the level 2A version 'B01' data. The 'B01' data are analyzed in more detail in the following sections.

Spectral Difference Analysis of 'B01' Data

Monthly mean images of the 'B01' TB data at 6.9 GHz and 10.7 GHz horizontal polarizations, and their difference computed as: $\Delta_{6H-10H} = TB_{6.9H} - TB_{10.7H}$, are shown in Figure 5. The TB images show good consistency between the 6.9 GHz and 10.7 GHz data over forests, indicating satisfactory removal of the 7 K offset. The difference image, Figure 5(c), shows geophysical features related primarily to variations in surface moisture, vegetation water content, and penetration depth and scattering influences in vegetation, deserts, and ice sheets, though these variations are smoothed to a large degree at the monthly time-scale. The figure also shows anomalously high Δ_{6H-10H} differences in the U. S. and scattered over the Middle East, some parts of Europe and Asia, and a few locations in South America and Africa. These 'hot spots' are caused by radio-frequency interference (RFI) from ground transmitters contaminating the AMSR-E data. The RFI observed in AMSR-E data over the U. S. has been discussed by Li et al. [2004]. In this paper we provide a summary of the AMSR-E observed global RFI statistics, but defer a more detailed discussion of global RFI identification and characteristics to a forthcoming paper [Njoku et al., 2004]. Due to the widespread RFI encountered at 6.9 GHz, and the likelihood of growth during the coming decade in worldwide RFI at both 6.9 GHz and 10.7 GHz, RFI identification and filtering has become a major priority for operational land algorithms.

Figure 6 shows histograms of the horizontally polarized spectral differences, Δ_{6H-10H} , of Figure 5(c) and also the vertically polarized spectral differences, Δ_{6V-10V} . The histograms are defined over four regions: World, U. S., Africa & Middle East, and Europe, as indicated by the boxes outlined in Figure 1. Only land data are included in the

histograms. Excluding the Greenland and Antarctic ice sheet areas makes little difference to the World histograms. Most data in the H-pol histograms lie between -6 K and 1 K, except for the U. S. The data in the V-pol histograms lie mainly in the -2.5 K to 4 K range. The histogram means and interquartile ranges (Table 3) show the influence of RFI over the U. S. The interquartile range (IQR) represents the range of the middle 50% of the data, and is used here instead of the standard deviation as a measure of dispersion since it is not affected by outliers with extreme values of RFI. The U. S. histograms are positively skewed with means of 1.76 K (H) and 4.18 K (V), reflecting the large amount of 6.9 GHz RFI in the U. S. (the spike at $\square_{6H-10H} = 30$ K indicates all points with $\square_{6H-10H} \geq 30$ K. The negative 'tails' of the Europe histograms indicate the presence of some 10.7 GHz RFI in that region. The spectral difference histogram characteristics are important in attempting to set thresholds for identification of RFI. However, the histograms do not show clear breaks between RFI-free and RFI-contaminated data, hence spectral differences alone are not clear indicators of RFI. Development of indices that have better RFI discrimination capabilities, using both means and standard deviations of spectral differences, is currently in progress [Njoku et al., 2004]. It is difficult to verify the locations and intensities of RFI in satellite observations due to the limited information available on the global distributions of transmitting sources in specific passbands. Some progress is being made, however, in identifying these sources over the U. S. [Kunkee, 2004].

Polarization Difference Analysis of 'B01' Data

The relative calibration between the vertical and horizontal polarizations at a given frequency is an important aspect of the instrument calibration. Calibration stability of the polarization difference is important for geophysical retrieval algorithms that use multi-polarization data. This calibration can also be evaluated by observations of AMSR-E data over forests. The polarization difference, $PD = TB_V - TB_H$, is expected to be close to zero over homogeneous tropical forests since the dense canopy approximates an unpolarized blackbody emitter and masks the underlying soil. The polarization

difference will deviate from zero if there is polarized scattering or emission in the vegetation or if the canopy is not completely opaque.

Figure 7 shows the July 2002 monthly average AMSR-E maps of PD for 6.9, 10.7, and 18.7 GHz (descending passes). The color scale is chosen to highlight the 0-4 K range (values ≥ 4 K are assigned the same color), which is the range of PD expected for dense vegetation. The images highlight the densely-vegetated regions of tropical and boreal forests. The forest PD values are generally close to but slightly greater than zero in these regions. (For bare soil surfaces at off-nadir viewing angles TB_V is generally significantly larger than TB_H , particularly for wetter and smoother surfaces.) The forest PD values are typically smaller at 18.6 GHz than at 6.9 GHz and 10.6 GHz, due to the increased canopy opacity at the higher frequency, which minimizes the polarizing effects of branches, trunks, and underlying surface.

To examine the polarization differences in more detail, Figure 8 shows time series plots of PD for 6.9, 10.7, 18.7, and 36.5 GHz at the forest sites of Salonga (Zaire) and Curua (Brazil) for the 3-month period June through August 2002. AMSR-E observes a given location approximately every other day at latitudes near the Equator. The time series generally fit expected patterns. The spread between the different frequency plots is less for the descending (1:30 am) than for the ascending (1:30 pm) passes, indicating a diurnal effect most likely linked to nonuniform temperatures and penetration depths in the canopy. The Brazil and Zaire plots look quite similar, though with more spectral divergence in Zaire, indicating little geographic variability in the forest calibration and brightness temperature characteristics. There is a 'sawtooth' pattern evident in the larger PD ascending plots (6.9 GHz and 10.7 GHz), and visible to a lesser degree in the higher frequencies and descending plots also. The site locations are viewed progressively across the swath for successive samples on subsequent days. Since the swath width is 1445 km, there is an approximately 50-minute time difference in local solar time across the swath at these latitudes. For a simple emissivity model of the surface, the brightness temperature at polarization p (V or H) is given by $TB_p = e_p T_S$, where T_S is the surface temperature and e_p is the emissivity. Thus, the polarization difference is $PD = TB_V - TB_H$

$= (e_V - e_H) T_S$. The sawtooth pattern could therefore be related to diurnal temperature variations in T_S , or possibly in $(e_V - e_H)$.

Table 4 shows the means and standard deviations of the time series plots for the three-month period at each site, for the ascending and descending passes. The means are plotted for clarity in Figure 9. The *PD* means at 36.5 GHz show slightly negative values for the ascending (1:30 pm) passes. From Figure 8, the negative values for the ascending passes are contributed to by the entire three-month period in Zaire, but mostly by the August period in Brazil. It is difficult to conclude whether this is a geophysical effect at 36.5 GHz (e.g., atmospheric signal) or represents a small calibration variation between the descending and ascending passes. However the effect is small (~ 0.5 K) and not significant enough to cause concern for land parameter retrieval algorithms. Calibration biases, if they exist, appear to be minimal in the 'B01' data, and the polarization differences over land are reasonably consistent with expectation. More extensive theoretical modeling and controlled radiometric measurements of forest canopies would be required to interpret these data further.

Seasonal Trends

The self-consistency and calibration stability of the brightness temperatures can be evaluated by plotting the time series data at different sites. Figures 10–12 show time series plots at sites 1, 3, 9, 10 and 19 (Figure 1 and Table 2). The two forest sites and the Antarctic site are temporally relatively stable and are therefore suitable as external calibration targets. Fifteen months of data are shown, covering the period June 2002 through August 2003, illustrating the annual cycle trends over the forest, desert, and ice sheet surface types. The TB data are shown for vertical polarization and descending passes only, minimizing the temporal variability of surface emissivity and temperature, respectively. Similar plots have been made for all sites listed in Table 2 as part of the continuing AMSR-E land calibration analysis, but are not shown here due to space limitations.

Figure 10 shows the mean TB plots at 6.9, 10.7 and 18.7 GHz for the forest (Mitu and Salonga) and desert (Western Desert and Simpson Desert) sites, determined by taking the average of the nine points in each daily extracted 3 x 3 array centered at the site locations. The adjustment of the 6.9 GHz TB level by 7 K is seen to have roughly equalized the 6.9 and 10.7 GHz TBs over the forests, though with a residual small positive bias at the Mitu site. The forest data show very little temporal variability over the annual cycle. The annual cycle is evident in the desert time series due mainly to the large annual variation in surface temperature over these deserts. Several low TB spikes are seen in the time series for the Simpson Desert. These are due to precipitation and surface wetting, indicating the occasionally intense rain in this desert region. The time series of TB standard deviations within each extracted 3 x 3 site are shown in Figure 11. It is notable that the forest sites show very low standard deviations, indicating that the sites are very homogeneous. Small spikes are seen, primarily at the 18 GHz frequency, indicating effects of clouds and precipitation variability across the sites. The desert site in Australia is much more homogeneous than that in Egypt, except for the occurrences of rain.

Figure 12 shows the mean and standard deviation time series for the site in Antarctica. This site, designated 'Dome C', is known for its extremely dry, cold, and low-wind atmospheric conditions, and stable surface emissivity conditions. It has therefore been considered a useful calibration site for polar-orbiting satellite sensors [Six, et al., 2004; Bingham and Drinkwater, 2000]. The mean time series, Figure 12 (a), shows the combined effects of the spectral emissivity differences and the annual temperature cycle. Increased volume scattering in the ice structure at shorter wavelengths causes the emissivity to decrease as the frequency increases, thereby lowering the brightness temperatures at the higher frequencies. At the same time, because the penetration depth increases with wavelength, the emission at the lower frequencies originates from deeper in the ice, thus sampling the colder temperature at depth. The emission at 36.5 GHz samples mainly the near-surface temperature. As a result, the annual TB variability at 6.9 GHz is quite small (less than 5 K) despite the large annual surface temperature variation. (The average surface air temperature at Dome C typically ranges from about -60°C in winter to -30°C in summer.) The standard deviations of Figure 12 (b) are indicative

mainly of the temperature variations across the spatial extent of the 3 x 3 grid point region at the different sampling depths.

Discussion and Conclusions

In this study we have investigated the AMSR-E spectral difference and polarization difference brightness temperatures and trends for a complete annual cycle over different land surfaces. Homogeneous and time-stable calibration regions of the globe were investigated primarily to examine the stability and self-consistency of the AMSR-E TBs. A high bias in the 6.9 GHz TB data was identified and adjusted in the early version of data processing. Examination of the current version of archived TB data (version 'B01') indicates that the data show good self-consistency for geophysical retrievals over land. A summary of the radio frequency interference problem was provided with reference to more detailed forthcoming studies. Several interesting features of the multifrequency AMSR-E brightness temperature characteristics over forests, deserts, and ice sheets have been discussed. Further work would be useful to better define the spectral scattering and volume emission characteristics of forest vegetation and ice sheets, and thus verify the observed spectral signatures. This would increase the value of homogeneous tropical forests and ice sheets as calibration targets for future radiometer missions.

References

Ashcroft, P. and Wentz, F. (2000) - *Algorithm Theoretical Basis Document (ATBD): AMSR Level 2A Algorithm* - RSS Technical Report 121599B-1, Remote Sensing Systems, Santa Rosa, CA.

Bingham, A. and Drinkwater, M. (2000) - *Recent changes in the microwave scattering properties of the Antarctic ice sheet*, IEEE Trans. Geosci. Rem. Sens., 38: 1810–1820.

Hollinger, J. P., Peirce, J. L. and Poe, G. (1990) - *SSM/I instrument evaluation*, IEEE Trans. Geosci. Rem. Sens., 28: 781–790.

Kawanishi, T., Sezai, T., Ito, Y., Imaoka, K., Takeshima, T., Ishido, Y., Shibata, A., Miura, M., Inahata, H. and Spencer, R. (2003) - *The Advanced Microwave Scanning Radiometer for the Earth Observing System (AMSR-E), NASDA's contribution to the EOS for global energy and water cycle studies*, IEEE Trans. Geosci. Rem. Sens., 41: 184–194.

Kunkee, D. (2004) (Personal communication).

Li, L., Njoku, E., Im, E., Chang, P. and St. Germain, K. (2004) - *A preliminary survey of radio-frequency interference over the U.S. in Aqua AMSR-E data*, IEEE Trans. Geosci. Rem. Sens., 42: 380–390.

Njoku, E., Koike, T., Jackson, T. and Paloscia, S. (2000) - *Retrieval of soil moisture from AMSR data*, in: *Microwave Radiometry for Remote Sensing of the Earth's Surface and Atmosphere* (Pampaloni, P. and Paloscia, S., Eds.), VSP, Utrecht.

Njoku, E., Jackson, T., Lakshmi, V., Chan, T. and Nghiem, S. (2003) - *Soil moisture retrieval from AMSR-E*, IEEE Trans. Geosci. Rem. Sens., 41: 215–229.

Njoku, E., Ashcroft, P. and Li, L. (2004) - *Statistics and global survey of radio-frequency interference in AMSR-E land observations*, (to be submitted to IEEE Trans. Geosci. Rem. Sens.).

Owe, M., De Jeu, R. and Walker, J. (2001) – *A methodology for surface soil moisture and vegetation optical depth retrieval using the microwave polarization difference index*, IEEE Trans. Geosci. Rem. Sens., 39: 1643–1654.

Paloscia, S., Macelloni, G., Sanit, E. and Koike, T. (2001) – *A multifrequency algorithm for the retrieval of soil moisture on a large scale using microwave data from SMMR and SSM/I satellites*, IEEE Trans. Geosci. Rem. Sens., 39: 1655–1661.

Parkinson, C. L. (2003) – *Aqua: An earth-observing satellite mission to examine water and other climate variables*, IEEE Trans. Geosci. Rem. Sens., 41: 172–183.

Ruf, C. S. (2000) – *Detection of calibration drifts in spaceborne microwave radiometers using a vicarious cold reference*, IEEE Trans. Geosci. Rem. Sens., 38: 44–52.

Shibata, A., Imaoka, K. and Koike, T. (2003) - *AMSR/AMSR-E level 2 and 3 algorithm developments and data validation plans of NASDA*, IEEE Trans. Geosci. Rem. Sens., 41: 195–203.

Six, D., Fily, M., Alvain, S., Henry, P. and Benoist, J.-P. (2004) - *Surface characterization of the Dome Concordia area (Antarctica) as a potential satellite calibration site using Spot 4/Vegetation instrument*, Rem. Sens. of Environ., 89: 83–94.

Tsai, W., Graf, J. E, Winn, C., Huddleston, J. N., Dunbar, S., Freilich, M. H., Wentz, F. J., Long, D. G. and Jones, W. L. (1999) – *Postlaunch sensor verification and calibration of the NASA Scatterometer*, IEEE Trans. Geosci. Rem. Sens., 37: 1517–1542.

Wan, Z. and Li, Z.-L. (1997) – *A physics-based algorithm for retrieving land-surface emissivity and temperature from EOS/MODIS data*, IEEE Trans. Geosci. Remote Sensing, 35: 980-996.

Wan, Z. (1999) – *MODIS land-surface temperature algorithm theoretical basis document (LST ATBD): version 3.3*,
(http://modis.gsfc.nasa.gov/data/atbd/atbd_mod11.pdf).

Wan, Z., Zhang, Y., Zhang, Q. and Li, Z.-L. (2004) – *Quality assessment and validation of the MODIS global surface temperature*, Int. J. Remote Sensing, 25: 261-274.

Wentz, F. J., Ashcroft, P. and Gentemann, C. (2001) – *Post-launch calibration of the TRMM Microwave Imager*, IEEE Trans. Geosci. Rem. Sens., 39: 415–422.

Wentz, F. J., Gentemann, C. and Ashcroft, P. (2003) – *On-orbit calibration of AMSR-E and the retrieval of ocean products*,

(http://www.ssmi.com/amsr/amsr_data_description.html), Remote Sensing Systems, Santa Rosa, CA.

Wentz, F. J (2004) - *Personal communication*, Remote Sensing Systems, Santa Rosa, CA.

Table 1 - AMSR-E nominal instrument characteristics.

Center frequency (GHz)	6.925	10.65	18.7	23.8	36.5	89.0
Bandwidth (MHz)	350	100	200	400	1000	3000
Sensitivity (K)	0.3	0.6	0.6	0.6	0.6	1.1
IFOV (km)	75 x 43	51 x 29	27 x 16	32 x 18	14 x 8	6 x 4
Sample spacing (km)	10 x 10	10 x 10	10 x 10	10 x 10	10 x 10	5 x 5
Integration time (ms)	2.5	2.5	2.5	2.5	2.5	1.2
Main-beam efficiency (%)	95.1	94.8	95.8	94.8	93.9	94.0
Beamwidth (deg)	2.2	1.5	0.8	0.92	0.42	0.19
Antenna diameter (m)	1.6					
Scan period (s)	1.5					
Antenna offset angle (deg)	47.5					
Earth-incidence angle (deg)	55					
Orbit altitude (km)	705					
Swath width (km)	1445					
Orbit type	Sun-synchronous, 1:30 pm equator crossing					
Orbit period (min)	98.8					
Sub-spacecraft velocity (km s ⁻¹)	6.76					

Table 2 – Locations of data extraction sites for brightness temperature trend analyses.

Site Name	Region	Surface Type	Center Latitude (deg)	Center Longitude (deg)
1. Simpson Desert	Central Australia	Desert	-24.5	137.0
2. Kalahari Desert	S.W. Botswana	Desert	-24.5	21.5
3. Western Desert	W. Egypt	Desert	26.5	26.5
4. Erg Chech	W. Algeria	Desert	26.5	-2.5
5. Bilma	E. Niger	Sahel	18.5	13.5
6. Tahoua	S.W. Niger	Sahel	14.0	5.0
7. Kayes	Mali/Senegal	Sahel	15.0	-12.0
8. Boumba	S.E. Cameroon	Tropical Forest	3.5	14.5
9. Salonga	Central Zaire	Tropical Forest	-1.5	21.5
10. Mitu	Colombia/Brazil	Tropical Forest	1.5	-69.5
11. Curua	Central Brazil	Tropical Forest	-8.5	-54.5
12. Boreas SSA	Saskatchewan, Canada	Boreal Forest	54.0	-104
13. Boreas NSA	Manitoba, Canada	Boreal Forest	56.0	-98
14. Bonanza Creek	Central Alaska	Boreal Forest	64.5	-148
15. Toolic Lake	N. Central Alaska	Tundra	68.5	-149.5
16. Little Washita SGP	Oklahoma	Grassland	36.0	-97.5
17. Lonoke Farm SCAN	Arkansas	Grassland	34.9	-91.9
18. Mongolian Plateau	S.E. Mongolia	Desert/Steppe	44.5	108.0
19. Dome C	Antarctica	Ice Sheet	75.1	123.4

Table 3 – Histogram statistics of 6.9 GHz minus 10.7 GHz brightness temperature spectral differences.

Region	Bounding Region Coordinates	Normalizing Factor (# of points)	Mean (K)		IQR (K)	
			V	H	V	H
World	Global	237,178	1.28	-2.05	2.72	3.21
U. S.	25 N to 49 N 125 W to 67 W	15,297	4.18	1.76	4.38	6.50
Africa	40 S to 40 N 20 W to 60 E	57,923	1.87	-2.28	1.75	2.52
Europe & Middle East	33 N to 60 N 20 W to 44 E	13,057	0.35	-2.77	1.94	2.0

Table 4 – Means and standard deviations of time polarization difference (PD) for the three-month period at each site, for ascending and descending passes.

Zaire (ascending)

	Mean	Std Dev
06V-H	2.2	0.6
10V-H	1.8	0.5
18V-H	0.4	0.3
36V-H	-0.2	0.3

Zaire (descending)

	Mean	Std Dev
06V-H	2.5	0.5
10V-H	2.4	0.4
18V-H	1.2	0.4
36V-H	1.1	0.5

Brazil (ascending)

	Mean	Std Dev
06V-H	1.9	0.7
10V-H	1.5	0.5
18V-H	0.7	0.4
36V-H	-0.1	0.4

Brazil (descending)

	Mean	Std Dev
06V-H	2.6	0.4
10V-H	2.5	0.4
18V-H	1.7	0.3
36V-H	1.6	0.3

Figure Captions

- Figure 1: Global map showing locations of data extraction sites for long-term brightness temperature trend and calibration monitoring, and U. S., Africa, and Europe regions for spectral difference histograms.
- Figure 2: Brightness temperatures (version 'X1') at the AMSR-E frequencies of 6.9, 10.7, 18.7 and 36.5 GHz, averaged over three months (June through August 2002) for sites: (a) Salonga, Zaire; (b) Curua, Brazil.
- Figure 3: Computed differences between the AMSR-E brightness temperatures with and without atmospheric effects (water vapor and oxygen) for different surface emissivities and precipitable water amounts. (Dots indicate the AMSR-E frequencies.)
- Figure 4: *Upper panels:* Time series of AMSR-E brightness temperatures and MODIS-derived land surface temperatures over the Zaire tropical forest site, for cloud-free days in the period July 2002 to February 2003. *Lower panels:* Derived emissivities obtained by normalizing the AMSR-E brightness temperatures by the MODIS land surface temperatures. Data from nighttime (descending) passes are shown.
- Figure 5: Monthly mean images of AMSR-E brightness temperatures (version 'B01') at horizontal polarization and for descending (nighttime) passes, (a) 6.9 GHz, (b) 10.7 GHz, and (c) their difference.
- Figure 6: Histograms of brightness temperature spectral differences (6.9 GHz minus 10.7 GHz) over land, (a) horizontal polarization, (b) vertical polarization.

- Figure 7: Monthly averaged polarization differences, $PD = TB_V - TB_H$ (K), for July 2002. (a) 6.9 GHz. (b) 10.6 GHz. (c) 18.6 GHz. The color scale is chosen to highlight the 0–4 K range.
- Figure 8: Time series plots of $PD = TB_V - TB_H$ for 6.9, 10.7, 18.7 and 36.5 GHz at forest sites in Zaire and Brazil, for ascending and descending orbits.
- Figure 9: Mean values of the polarization differences (PD) (Table 4) plotted as a function of frequency at the Zaire and Brazil forest sites, for ascending and descending passes.
- Figure 10: Time series means of brightness temperatures within 3 x 3 (75 km²) grid area (vertical polarization, descending passes) at forest and desert sites (sites 1, 3, 9 and 10 of Table 1).
- Figure 11: Time series standard deviations of brightness temperatures within 3 x 3 (75 km²) grid area (vertical polarization, descending passes) at forest and desert sites (sites 1, 3, 9 and 10 of Table 1).
- Figure 12: Time series brightness temperatures at Dome C, Antarctica: (a) means, (b) standard deviations, within 3 x 3 (75 km²) grid area (vertical polarization, descending passes).

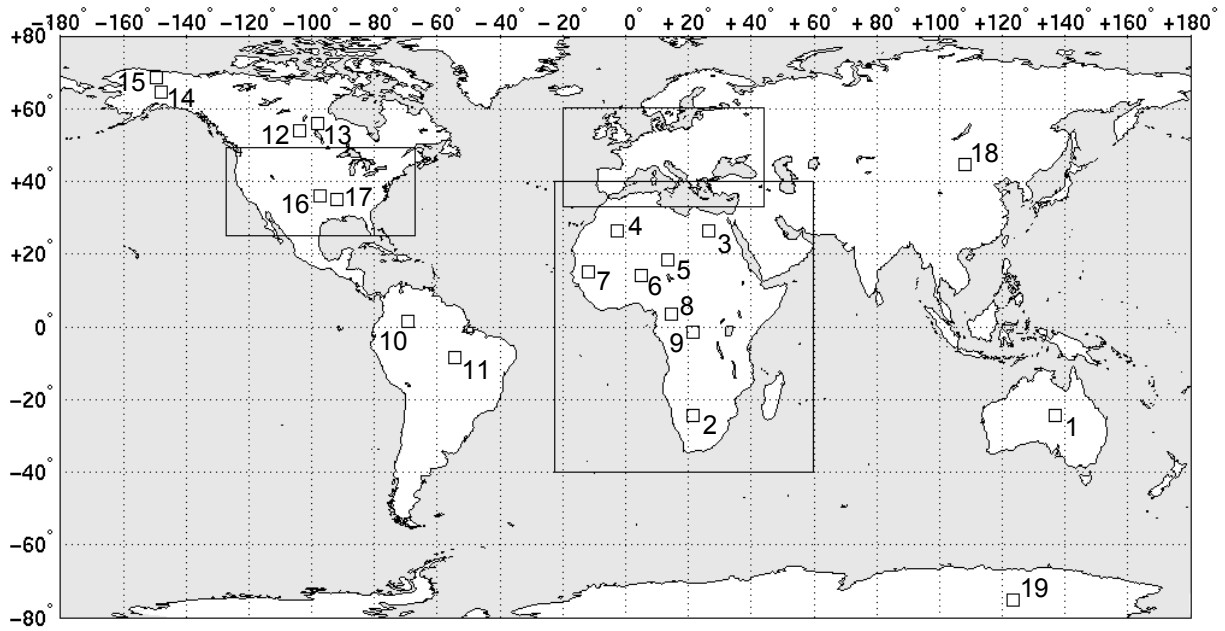


Figure 1: Global map showing locations of data extraction sites for long-term brightness temperature trend and calibration monitoring, and U. S., Africa, and Europe regions for spectral difference histograms.

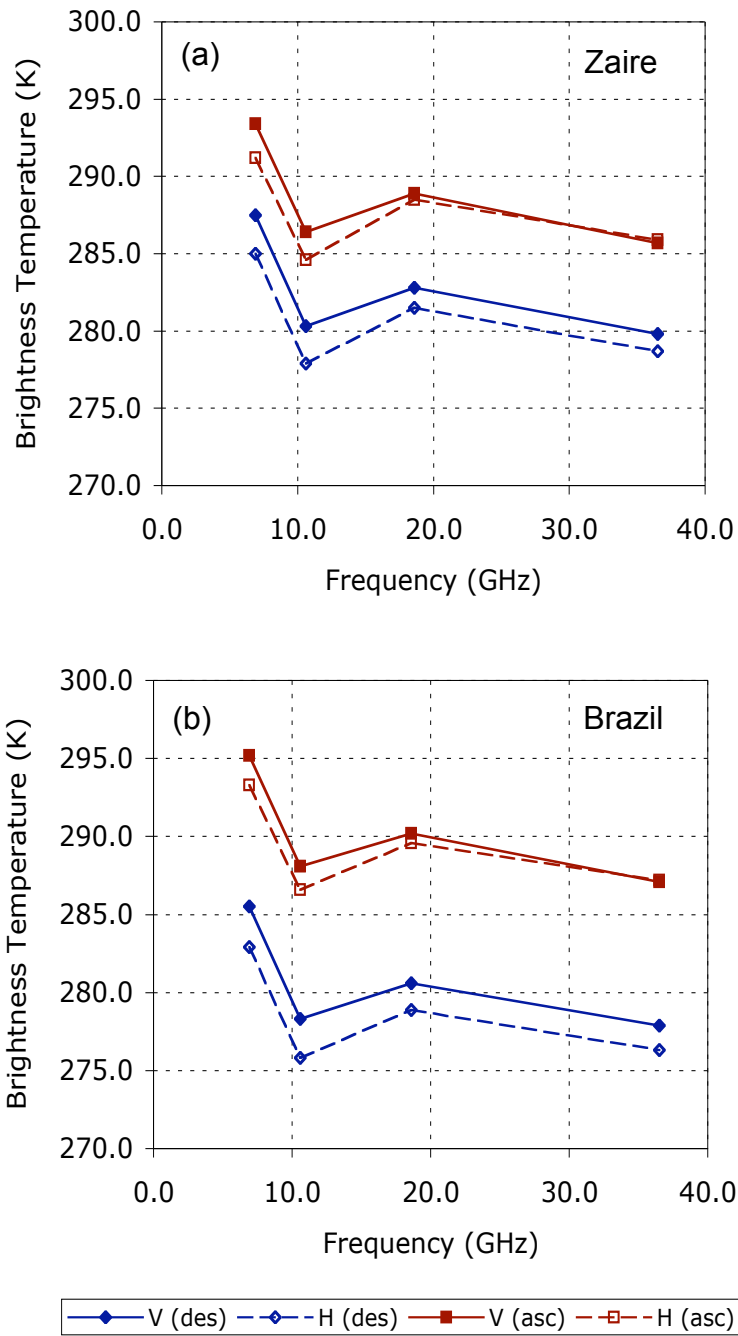


Figure 2: Brightness temperatures (version 'X1') at the AMSR-E frequencies of 6.9, 10.7, 18.7 and 36.5 GHz, averaged over three months (June through August 2002) for sites: (a) Salonga, Zaire; (b) Curua, Brazil.

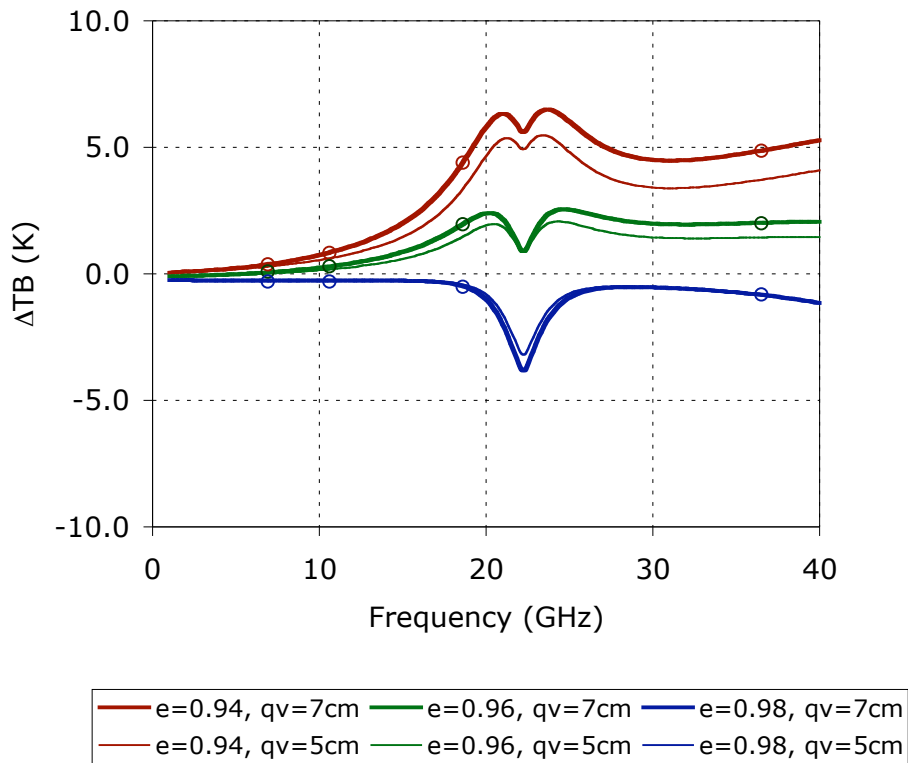


Figure 3: Computed differences between AMSR-E brightness temperatures with and without atmospheric effects (water vapor and oxygen), for different surface emissivities ($e = 0.94$ to 0.98) and precipitable water amounts ($q_v = 5$ and 7 cm). (Circles indicate the AMSR-E frequencies.)

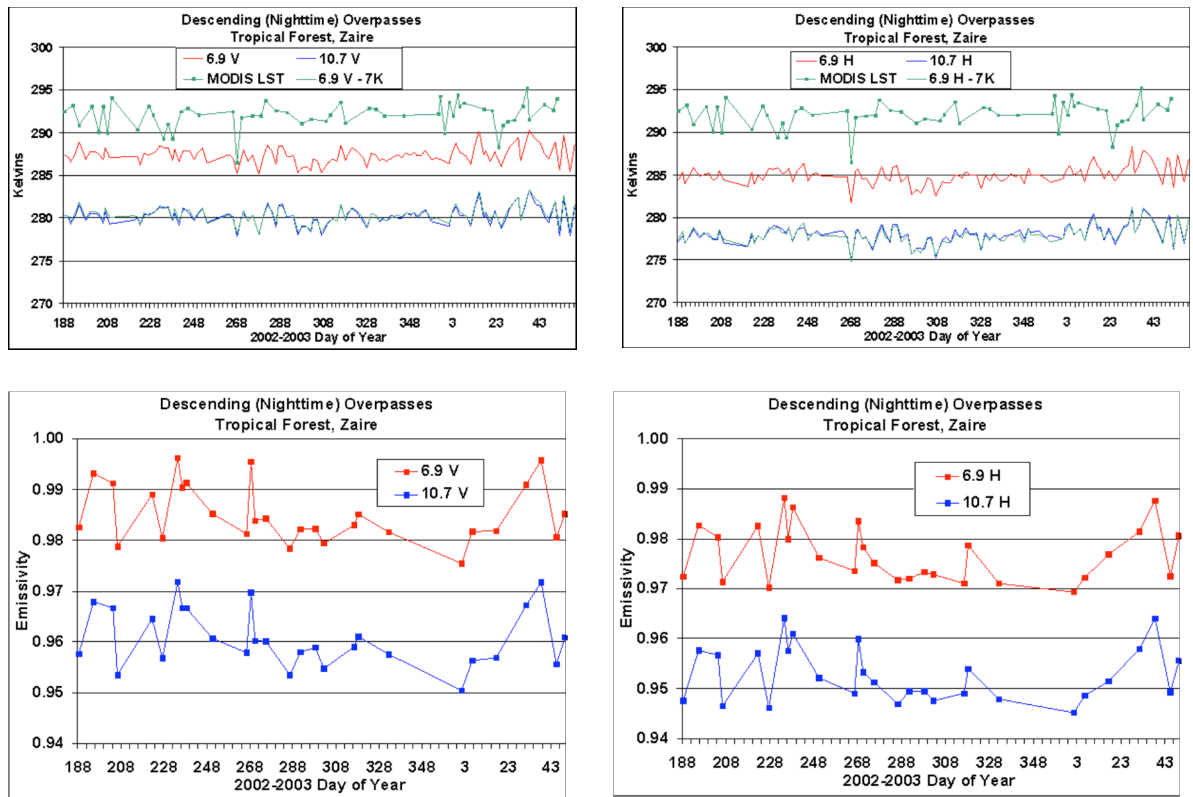


Figure 4: *Upper panels:* Time series of AMSR-E brightness temperatures and MODIS-derived land surface temperatures over the Zaire tropical forest site, for cloud-free days in the period July 2002 to February 2003. *Lower panels:* Derived emissivities obtained by normalizing the AMSR-E brightness temperatures by the MODIS land surface temperatures. Data from nighttime (descending) passes are shown.

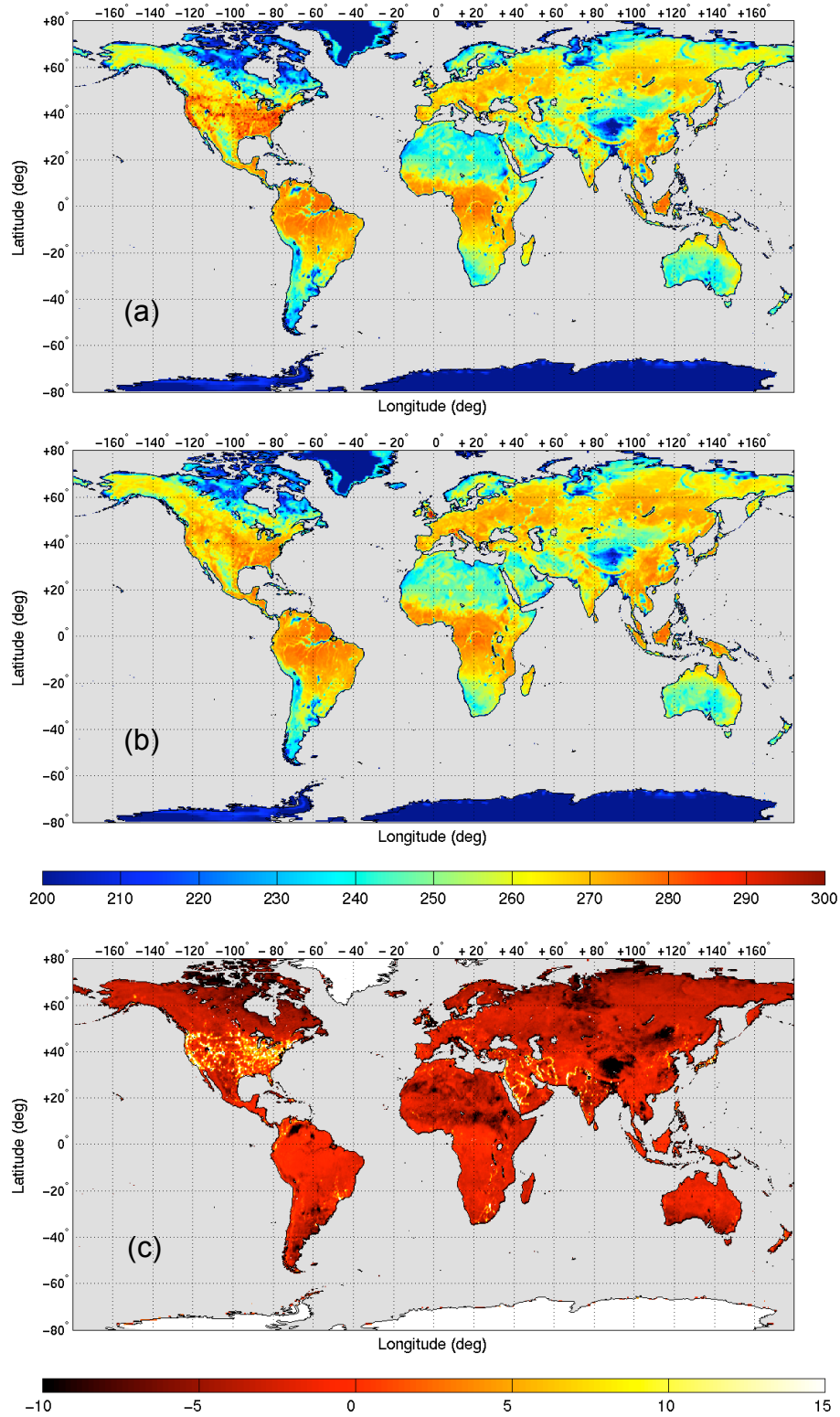
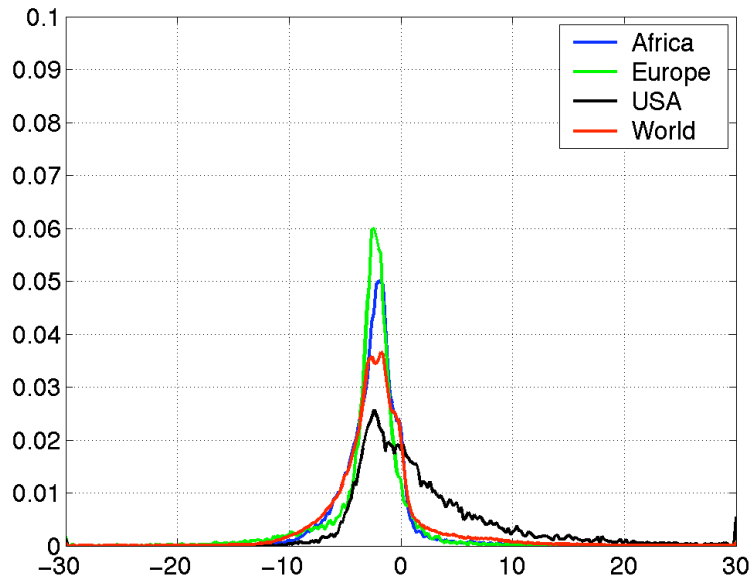
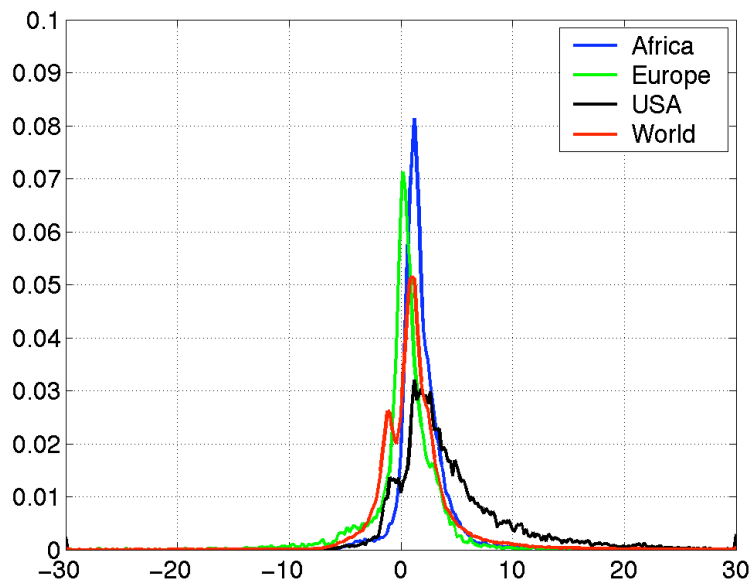


Figure 5: Monthly mean images of AMSR-E brightness temperatures (version 'B01') at horizontal polarization for descending (nighttime) passes, (a) 6.9 GHz, (b) 10.7 GHz, and (c) the difference (6.9 GHz minus 10.7 GHz). Units are in Kelvins.



(a) Horizontal



(b) Vertical

Figure 6: Histograms of brightness temperature spectral differences (6.9 GHz minus 10.7 GHz) over land, (a) horizontal polarization, (b) vertical polarization.

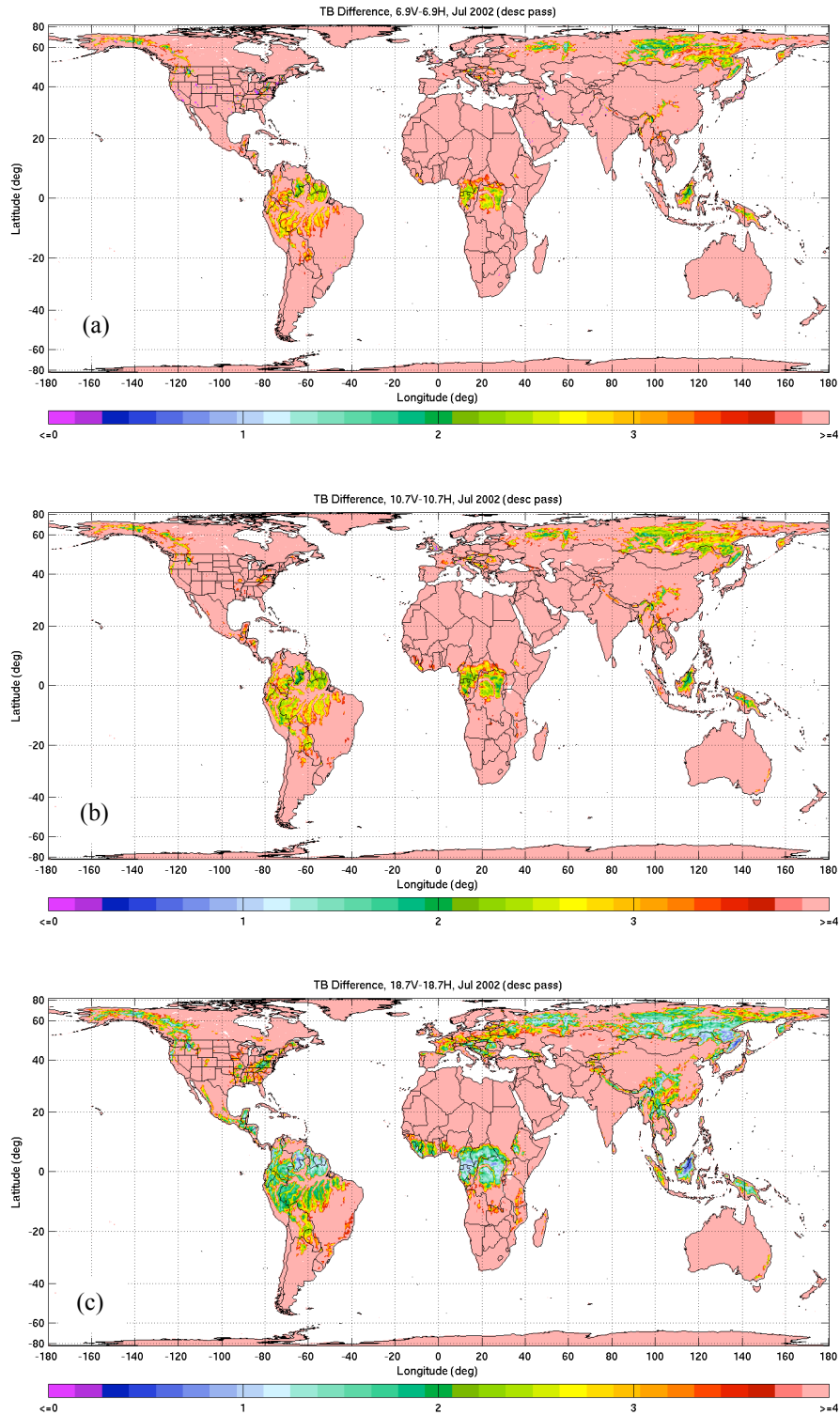


Figure 7: Monthly averaged polarization differences, $PD = TB_V - TB_H$ (K), for July 2002. (a) 6.9 GHz. (b) 10.6 GHz. (c) 18.6 GHz. The color scale is chosen to highlight the 0–4 K range.

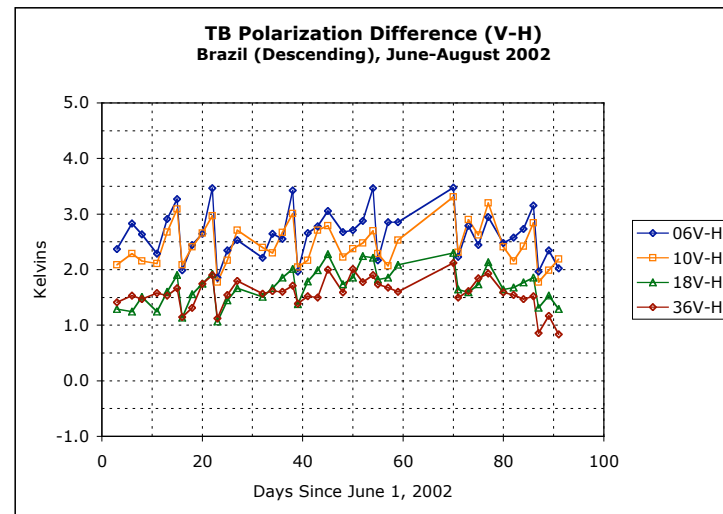
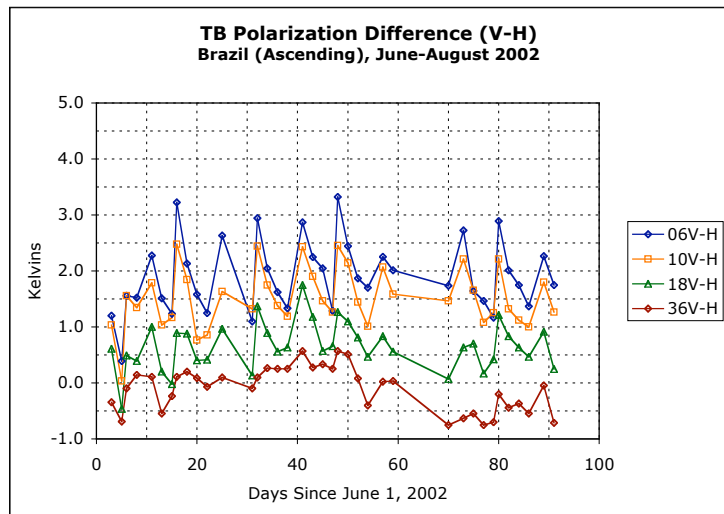
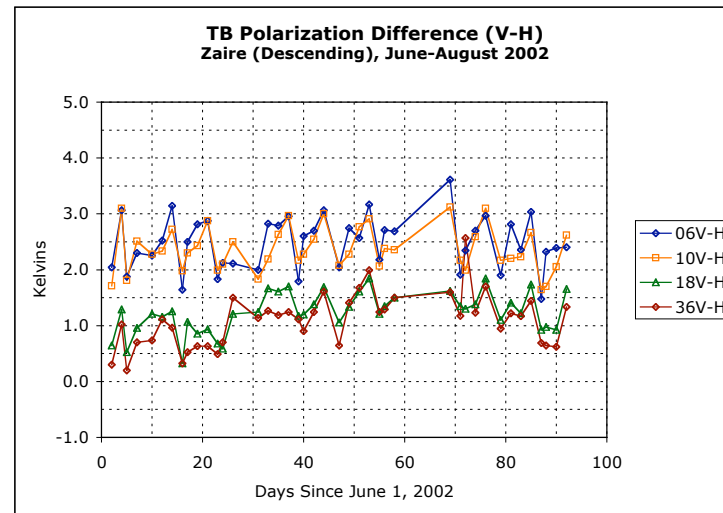
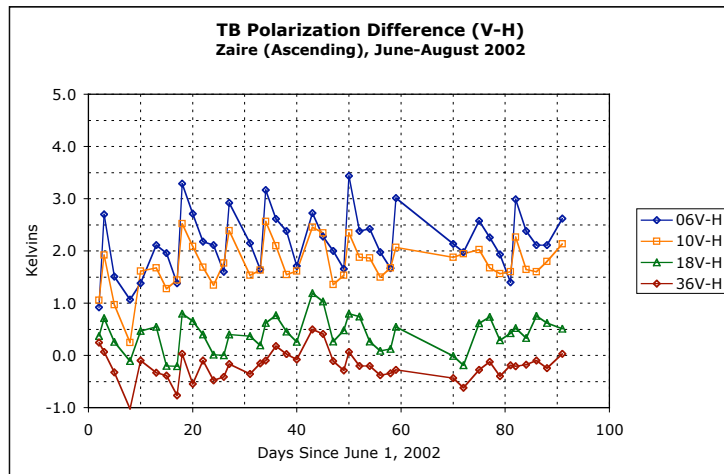


Figure 8: Time series plots of $PD = TB_V - TB_H$ for 6.9, 10.7, 18.7 and 36.5 GHz at forest sites in Zaire and Brazil, for ascending and descending orbits.

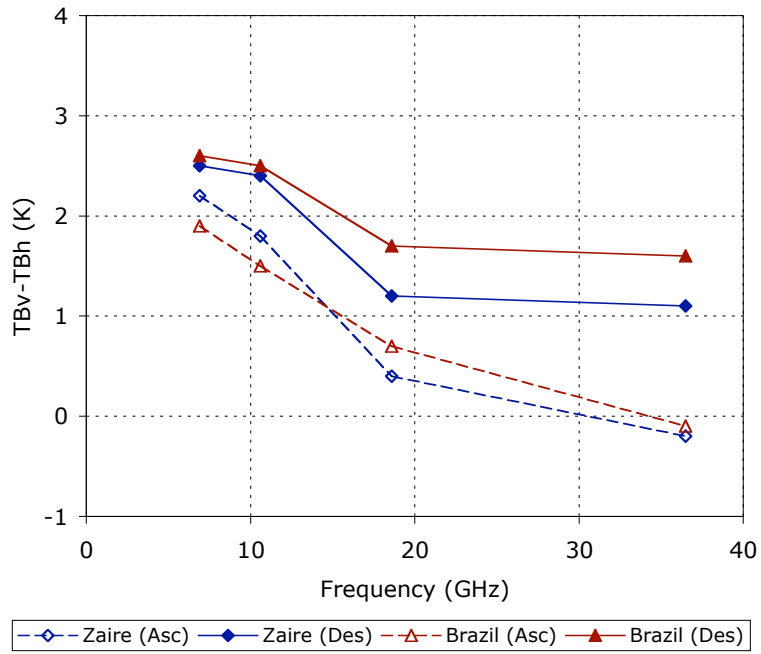


Figure 9. Mean values of the polarization differences (PD) (Table 4) plotted as a function of frequency at the Zaire and Brazil forest sites, for ascending and descending passes.

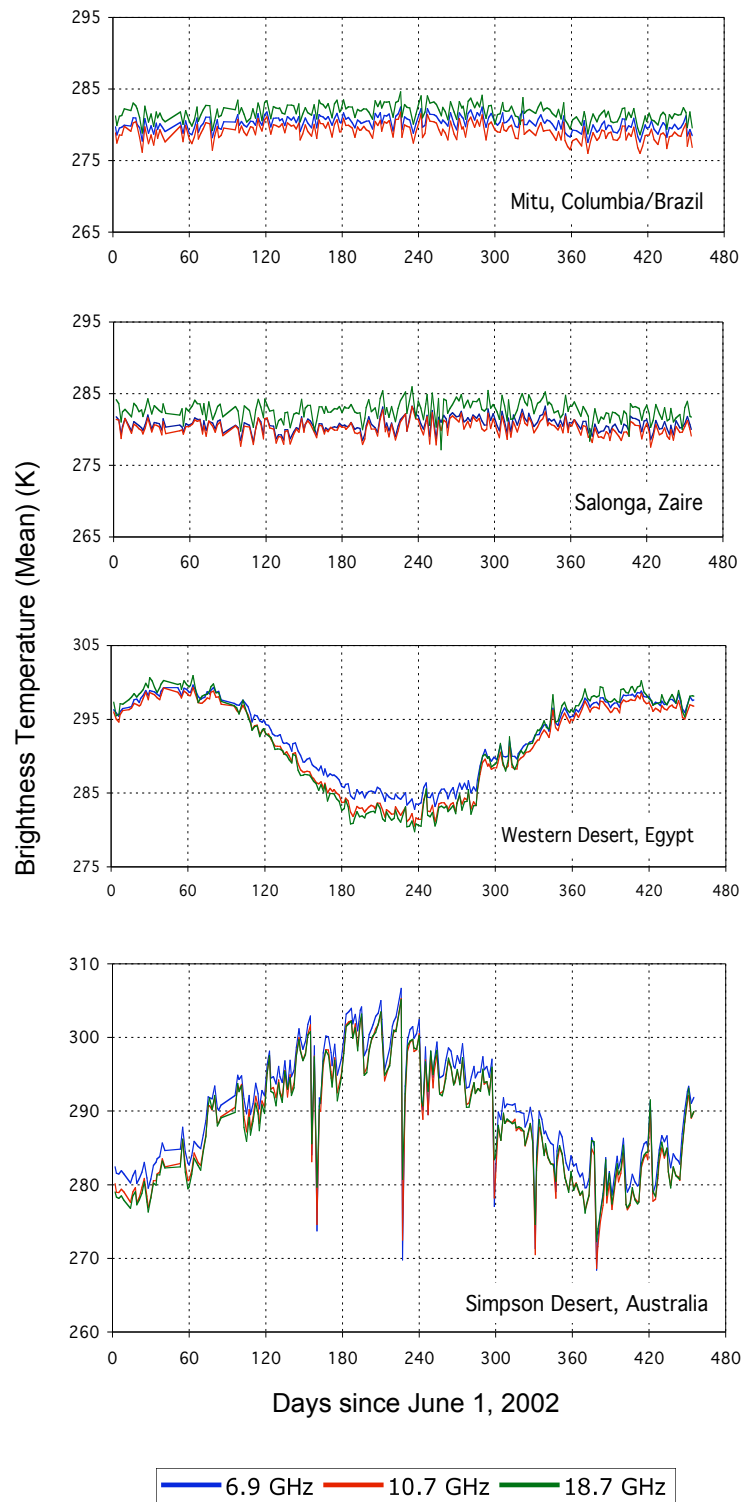


Figure 10. Time series means of brightness temperatures within 3x3 (75 km²) grid area (vertical polarization, descending passes) at forest and desert sites (1, 3, 9 and 10 of Table 1).

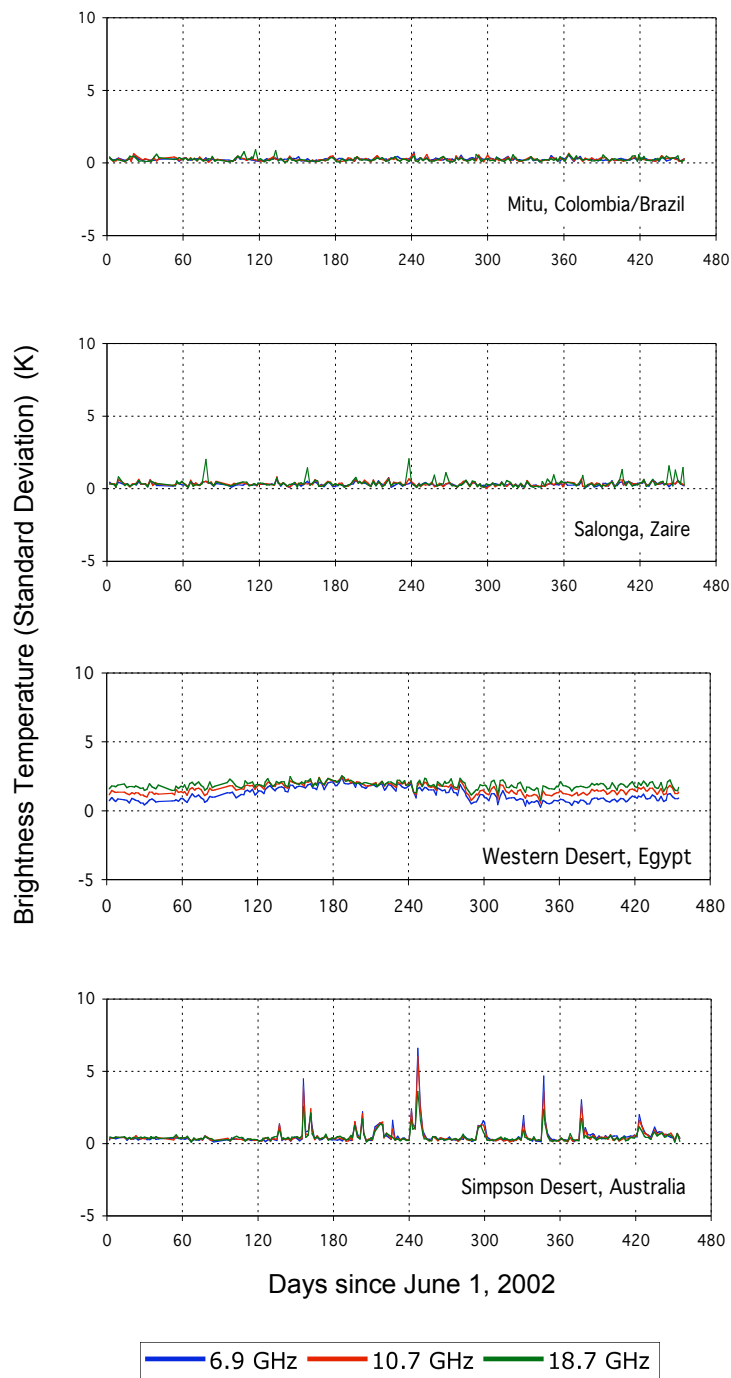


Figure 11. Time series standard deviations of brightness temperatures within 3x3 (75 km²) grid area (vertical polarization, descending passes) at forest and desert sites (1, 3, 9 and 10 of Table 1).

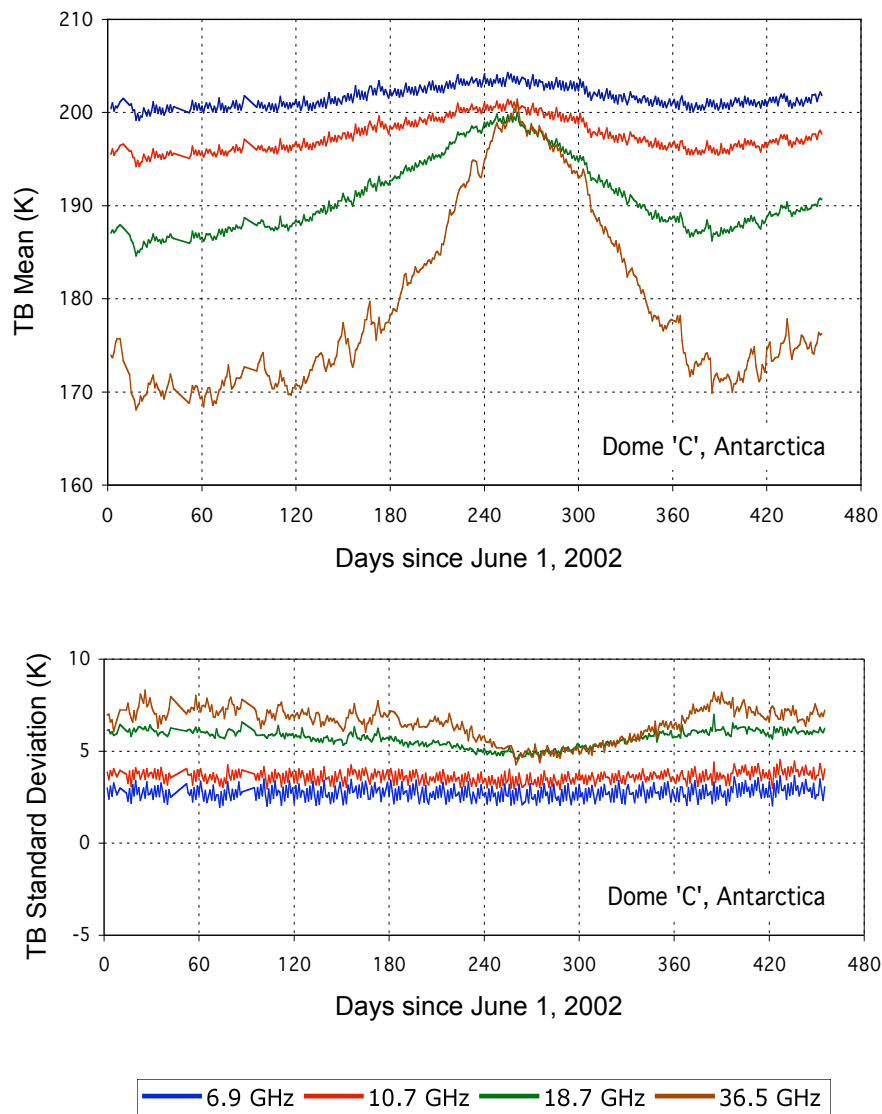


Figure 12. Time series brightness temperatures at Dome C, Antarctica: (a) means, (b) standard deviations, within 3x3 (75 km²) grid area (vertical polarization, descending passes).